

# Resistive relaxation of a magnetically confined mountain on an accreting neutron star

M. Vigeliu<sup>1\*</sup> and A. Melatos<sup>1</sup>

<sup>1</sup> *School of Physics, University of Melbourne, Parkville, VIC 3010, Australia*

Submitted to MNRAS

## ABSTRACT

Three-dimensional numerical magnetohydrodynamic (MHD) simulations are performed to investigate how a magnetically confined mountain on an accreting neutron star relaxes resistively. No evidence is found for non-ideal MHD instabilities on a short time-scale, such as the resistive ballooning mode or the tearing mode. Instead, the mountain relaxes gradually as matter is transported across magnetic surfaces on the diffusion time-scale, which evaluates to  $\tau_1 \sim 10^5 - 10^8$  yr (depending on the conductivity of the neutron star crust) for an accreted mass of  $M_a = 1.2 \times 10^{-4} M_\odot$ . The magnetic dipole moment simultaneously reemerges as the screening currents dissipate over  $\tau_1$ . For nonaxisymmetric mountains, ohmic dissipation tends to restore axisymmetry by magnetic reconnection at a filamentary neutral sheet in the equatorial plane. Ideal-MHD oscillations on the Alfvén time-scale, which can be excited by external influences, such as variations in the accretion torque, compress the magnetic field and hence decrease  $\tau_1$  by one order of magnitude relative to its standard value (as computed for the static configuration). The implications of long-lived mountains for gravitational wave emission from low-mass X-ray binaries are briefly explored.

**Key words:** accretion, accretion disks – stars: magnetic fields – stars: neutron – pulsars: general.

## 1 INTRODUCTION

Observations suggest that the magnetic dipole moment of accreting neutron stars in X-ray binaries,  $\mu$ , decreases with accreted mass,  $M_a$  (Taam & van de Heuvel 1986; van den Heuvel & Bitzaraki 1995), possibly through magnetic screening or burial (Bisnovatyi-Kogan & Komberg 1974; Romani 1990; Payne & Melatos 2004; Lovelace et al. 2005). During the burial process, the accreted plasma is channeled onto the magnetic poles of the neutron star, whence it spreads equatorwards, thereby distorting the frozen-in magnetic flux (Melatos & Phinney 2001). Quasistatic sequences of ideal-magnetohydrodynamic (ideal-MHD) equilibria describing how burial proceeds were computed by Payne & Melatos (2004) (hereafter PM04). These authors found that the magnetic field is compressed into an equatorial belt, which confines the accreted mountain at the poles.

Surprisingly, the distorted equilibrium magnetic fields resulting from burial are stable in ideal MHD. In an axisymmetric analysis, Payne & Melatos (2007) (hereafter PM07) found that the mountain, when perturbed, oscillates radially and laterally in a superposition of global Alfvén and

compressional modes, but it remains intact. Of course, an axisymmetric analysis neglects important toroidal modes. Vigeliu & Melatos (2008c) (hereafter VM08) found that the axisymmetric configuration is unstable to the undulating submode of the three-dimensional Parker instability in spherical geometry. Again though, while the hydromagnetic structure reconfigures itself globally, the mountain remains confined to the magnetic poles once the instability saturates.

PM04, PM07, and VM08 considered ideal-MHD equilibria. However, magnetic burial creates steep magnetic gradients, which relax resistively. A conservative estimate of the relative importance of nonideal effects can be arrived at by assuming that the electrical resistivity in the outer crust is dominated by electron-phonon scattering. Under this assumption, resistive relaxation arrests the growth of a mountain when the accreted mass exceeds  $\sim 10^{-5} M_\odot$  (Brown & Bildsten 1998; Cumming et al. 2004; Melatos & Payne 2005). Resistive instabilities, like the global tearing mode or the local gravitational mode (Furth et al. 1963), grow faster than the simple resistive time-scale. Three-dimensional modes like the resistive ballooning mode, which grows if the pressure gradient is parallel to the field line curvature, may rapidly destroy the confinement of the mountain.

During the early stages of accretion, the moun-

\* E-mail: mvigeliu@physics.unimelb.edu.au

tain might be disrupted on the Alfvén time scale by the ideal-MHD ballooning mode (Litwin et al. 2001). Vigeliu & Melatos (2008b) and Vigeliu (2008) show that equatorial magnetic stresses stabilize the configuration and generally prevent disruption in the high- $M_a$  regime. These authors then continue to solve the initial value problem by injecting plasma into an initially homogeneous background (with  $M_a = 0$ ) threaded by a dipolar field. They find no evidence for a growing instability in the low- $M_a$  regime. In this article, we investigate further how resistive relaxation competes with accretion at different accretion rates.

The main aim of this article is to test if resistive instabilities disrupt the mountain on time-scales comparable to the accretion time-scale. The article is divided into six sections. Section 2 introduces the numerical setup used in our simulations, section 3 describes the dynamics of the resistive relaxation, and section 4 characterizes the magnetic field structure. In section 5, we evaluate the resistive relaxation time as a function of accretion parameters. In section 6, we study how rapidly the magnetic field reemerges after accretion stops. We discuss our results in section 7, focussing on the ramifications for gravitational wave emission from accreting neutron stars.

## 2 NUMERICAL MODEL

### 2.1 Grid and units

The simulations in this paper employ the parallel, ideal-MHD solver ZEUS-MP (Hayes et al. 2006), extended to include resistive effects, as described in appendix A. All the simulations are carried out in a spherical polar coordinate system  $(r, \theta, \phi)$ , where  $r$  is logarithmically stretched as described in PM07 and VM08. To handle the disparate radial and lateral length-scales, we set up a downscaled neutron star with  $M_* = 1.01 \times 10^{-5} M_\odot$  and  $R_* = 2.7 \times 10^3$  cm, such that the curvature  $a = R_*/h_0 = 50$  is still large while the hydrostatic scale height  $h_0 = 53.8$  cm (defined in PM04) is preserved. We justify this approach by noting that the small- $M_a$  analytic solution depends on  $M_*$  and  $R_*$  only through the combination  $h_0$  (PM04). The downscaling transformation was employed in Payne & Melatos (2007) and VM08 and validated by Vigeliu & Melatos (2008b) in the large- $M_a$  regime.

Throughout this paper we fix  $\mu_0 = G = c_s = h_0 = 1$ , such that the base units (in cgs) for mass, magnetic field, time, and resistivity become  $M_0 = h_0 c_s^2 / G = 8.1 \times 10^{24}$  g,  $B_0 = [\mu_0 c_s^4 / (G h_0^2)]^{1/2} = 7.2 \times 10^{17}$  G,  $\tau_0 = h_0 / c_s = 5.4 \times 10^{-7}$  s, and  $\eta_0 = \tau_0^{-1} = 1.86 \times 10^6$  s $^{-1}$  respectively. The characteristic mass (PM04) then evaluates to  $M_c = 6.2 \times 10^{-15} M_\odot$  for the downscaled star.

### 2.2 Initial and boundary conditions

Our aim in this paper is to examine the influence of a finite conductivity on magnetic mountain equilibria in 2.5 and 3 dimensions. Axisymmetric equilibria are imported from the Grad-Shafranov (GS) solver developed by PM04. Non-axisymmetric equilibria are imported from ZEUS-MP after the transient, three-dimensional Parker instability saturates (VM08). All our simulations are isothermal (XISO=.true.).

Boundary conditions are enforced in ZEUS-MP by ghost cells framing the active grid. Our choice of a spherical polar grid requires periodic boundary conditions at the  $\phi$  boundaries [ikb.niks(1)=4 and ikb.noks(1)=4]. The  $\theta = \pi/2$  boundary is reflecting [obj.nojs(1)=5], with  $v_\perp = \mathbf{B}_\parallel = 0$ . The line  $\theta = 0$  is also reflecting [ijb.nijs(1)= -1], with tangential magnetic field ( $v_\perp = \mathbf{B}_\perp = 0$ ). Additionally, the toroidal component  $B_\phi$  reverses at  $\theta = 0$ , i.e.  $B_\phi(-\theta) = B_\phi(\theta)$ . The outer boundary at  $r = R_m$  is a zero-gradient boundary [oib.nois(1)= 2]. The magnetic field at  $r = R_*$  is line-tied by fixing the plasma variables [iib.niis(1)= 3] at this boundary:  $\mathbf{B}$  is dipolar and  $\rho$  is kept several orders of magnitudes higher than the active grid values in order to realise an impenetrable surface.

### 2.3 Resistivity

The electrical conductivity  $\sigma$  is a key input into the models presented in this article. In the outer crust, all transport processes are dominated by electrons scattering off phonons and impurities [for a recent review compare Chamel & Haensel (2008)] and  $\sigma$  can be derived from the scattering frequencies in the relaxation time approximation. For temperatures below the Umklapp temperature ( $T_U \approx 10^7$  K), electron-phonon scattering is suppressed and the conductivity must be attributed to impurities (Cumming et al. 2001, 2004). In rapid accretors ( $\dot{M} \gtrsim 10^{-11} M_\odot \text{ yr}^{-1}$ ), one finds  $T \gtrsim 10^8$  K and phonon scattering dominates, provided the impurity concentration satisfies  $Q \lesssim 1$ . In accreting neutron stars,  $Q$  is set by the composition of the ashes produced in steady state nuclear burning at low densities. Schatz et al. (1999) find a large variety of nuclei in the crust so the impurity factor is high ( $Q \approx 100$ ). They argue that impurity scattering therefore dominates, except for very rapid accretors ( $Q \sim 1$  for  $\dot{M} \gtrsim 30 \dot{M}_{\text{Edd}}$ ). On the other hand, Jones (2004) noted that, if the primordial crust is completely replaced by heterogeneous accreted matter, a temperature-independent conductivity dominates electron scattering and one finds  $Q \gg 1$ . Most authors (Konar & Bhattacharya 1997; Cumming et al. 2001, 2004; Pons & Geppert 2007) assume  $Q \ll 1$ , as do we.

Neglecting impurities, Potekhin et al. (1999) compute the frequency of electron-ion scattering in liquid and solid Fe matter for a variety of temperatures and densities. Chamel & Haensel (2008) present a computation of  $\sigma$  (including impurity scattering) for an accreted crust model (Haensel & Zdunik 1990a), finding  $23 \leq \log_{10}(\sigma/\text{s}^{-1}) \leq 27.4$  for  $T = 10^7$  K and  $10^9 \leq \rho[\text{gcm}^{-3}] \leq 10^{13}$  (note that this density range covers the whole outer crust including neutron drip). Cumming et al. (2004) find similar values for an accreted crust, viz.  $\sigma_p = 1.8 \times 10^{25} \text{ s}^{-1} (\rho_{14}^{7/6} / T_8^2)$  for electron-phonon and  $\sigma_Q = 4.4 \times 10^{25} \text{ s}^{-1} \rho_{14}^{1/3}$  for impurity scattering (provided  $Q = 1$ ).

To model a realistic star, we choose the electrical resistivity to be  $1.3 \times 10^{-27} \text{ s} \leq \eta_r \leq 1.3 \times 10^{-24} \text{ s}$ , covering the range quoted in the previous paragraph. Throughout this paper, we also run simulations with artificially high values of  $\eta$ , in the range  $1.3 \times 10^{-27} \leq (\eta/1 \text{ s}) \leq 9.2 \times 10^{-11}$ , in order to accelerate resistive processes and observe their evolution over a computationally practical time interval.

For simplicity, we assume an isothermal equation of

**Table 1.** Simulation parameters.  $\eta$  measures the resistivity in terms of the realistic value  $\eta_r = 1.3 \times 10^{-27}$  s and also determines the Lundquist number  $Lu = \tau_D/\tau_A$ , i.e. the ratio of the resistive time-scale  $\tau_D$  to the Alfvén time-scale  $\tau_A$ . Models A–D are axisymmetric; models E–H are nonaxisymmetric. All models are for  $M_a = M_c$ .

Model	$\log_{10}(\eta/\eta_r)$	$Lu$	axisymmetric
A	1	$5.7 \times 10^{15}$	yes
B	14.9	$8.0 \times 10^0$	yes
C	15.9	$8.0 \times 10^{-1}$	yes
D	16.9	$8.0 \times 10^{-3}$	yes
E	1	$2.99 \times 10^{14}$	no
F	14.9	$4.25 \times 10^3$	no
G	15.9	$4.25 \times 10^2$	no
H	16.9	$4.25 \times 10^1$	no

state throughout this article. During the late stages of accretion ( $M_a \gtrsim 10^{-3} M_\odot$ ), however, the magnetic mountain mass is comparable to the mass of the neutron star crust and the model mountain contains a wide range of densities and temperatures as a function of depth. Pycnonuclear reactions in the deep regions ( $\rho \gtrsim 10^{12} \text{ g cm}^{-3}$ ) feed thermal energy into an adiabatic mountain. The assumption of isothermality breaks down and a realistic equation of state for non-catalyzed matter is required (Haensel & Zdunik 1990a). In particular, the accreted material is expected to solidify at densities  $\gtrsim 10^8 \text{ g cm}^{-3}$  (Haensel & Zdunik 1990b) and will sink into the crust, which needs to be modelled as an elastic solid (Ushomirsky et al. 2000). In a self-consistent model, the electrical conductivity will be computed as a function of  $\rho$  and  $T$ . Furthermore, a strong magnetic field ( $B \gg 10^9$  G) breaks the symmetry of electron transport processes and causes an anisotropic conductivity (Potekhin 1999). The effect of a realistic equation of state is subject of current work and the results will be presented elsewhere.

In light of the discussion above, it is not immediately obvious at what location in the crust  $\sigma$  needs to be evaluated. In the end, however, we note that there are other deficiencies in our model which outweigh the uncertainties in the conductivity (most notably, sinking). In the context of this article, we therefore treat  $\sigma$  as a fiducial parameter. In particular, we will show how the resistive relaxation time scales with  $\sigma$  in section 5.

### 3 RESISTIVE INSTABILITIES

In general, MHD systems with a finite conductivity exhibit a plethora of resistive instabilities acting on time-scales much shorter than the diffusion time-scale (Lifschitz 1989; Biskamp 1993). Our first task is to find out if such instabilities are present here and on what time-scales they act. Table 1 lists the simulations performed to this end. We track the evolution of the mass ellipticity  $\epsilon$  as a convenient way to parametrize the evolution of the global hydromagnetic structure (VM08).

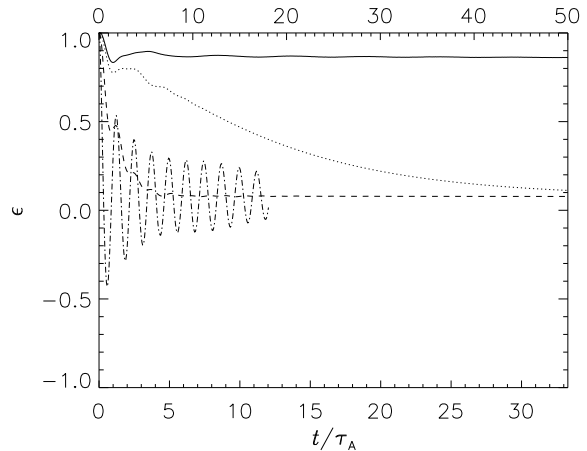


**Figure 1.** Evolution of mass ellipticity  $\epsilon$  for different Lundquist numbers (from top to bottom)  $Lu = 5.7 \times 10^{15}, 8, 0.8, 8 \times 10^{-3}$  (solid, dotted, dashed, dash-dotted) for the axisymmetric models A–D with  $M_a = M_c$ . The time is measured in units of the Alfvén time (bottom axis). The top axis measures the time in units of the diffusion time for model C. Clearly,  $\epsilon$  decays on the diffusive time-scale.

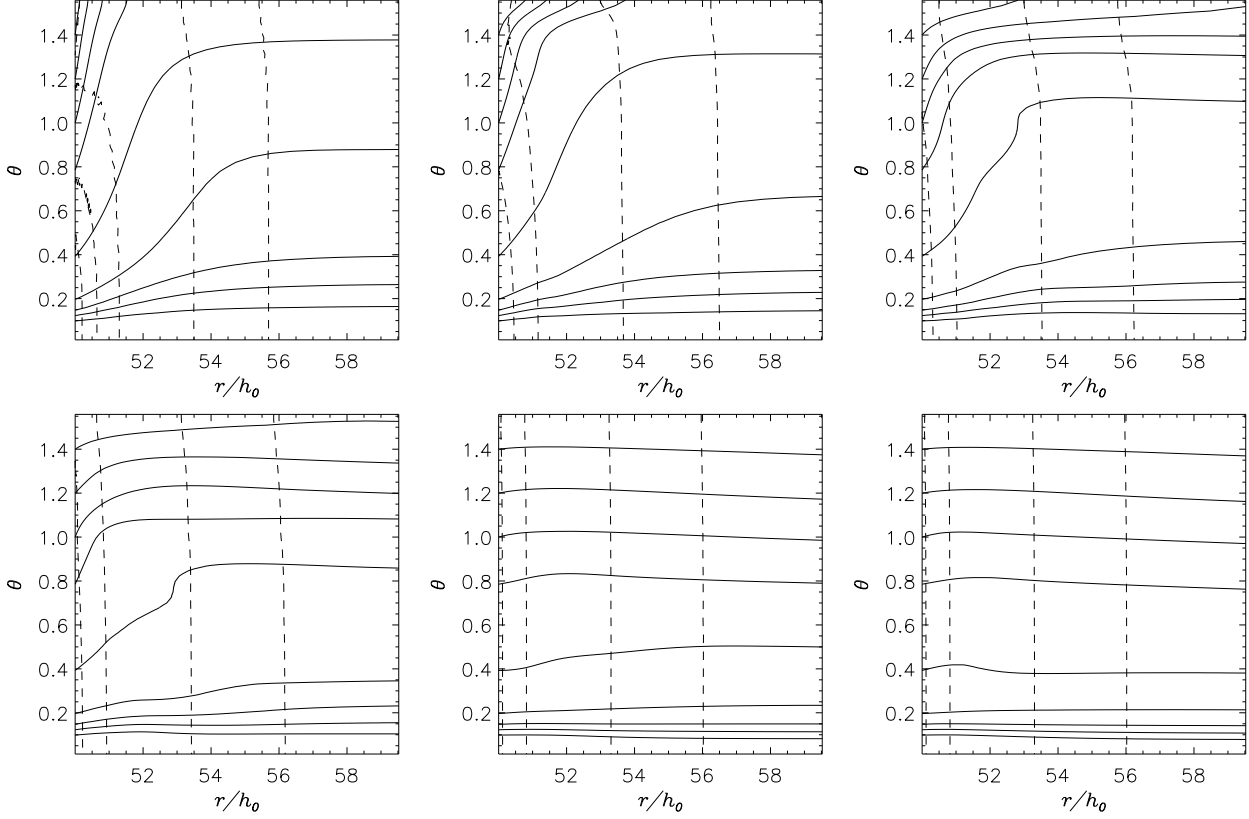
#### 3.1 Axisymmetric dynamics

Fig. 1 displays  $\epsilon$  as a function of time for models A–D in table 1. In order to find out if a genuine instability grows on an  $e$ -folding time-scale  $\tau_l < \tau_D$ , we artificially increase  $\eta$  and hence the Lundquist number  $Lu = \tau_D/\tau_A$  (models B–D). Here,  $\tau_A = L\rho^{1/2}/B$  and  $\tau_D = L^2\sigma$  denote the Alfvén and the diffusion time-scales, respectively,  $\sigma$  is the electrical conductivity and  $L = (|\mathbf{B}|/|\nabla^2\mathbf{B}|)^{1/2}$  is a characteristic length-scale. Clearly,  $L$ ,  $\tau_A$ , and  $\tau_D$  are functions of position and time. We minimize  $L$  and  $\tau_A$  over the integration volume, finding (for the axisymmetric models)  $L = 1.05 \times 10^{-3} h_0$  and  $\tau_A = 105\tau_0$  respectively.

During the first oscillation cycle in model B ( $Lu = 8$ ),  $\epsilon$  declines more steeply than in model A before tapering off. This behaviour becomes more distinct in model C ( $Lu = 0.8$ ), where  $\epsilon$  decreases rapidly, then plateaus when the equatorward motion of the mountain stops and subsequently reverses. This cycle of decline followed by plateauing repeats several times while  $\epsilon$  tends to zero overall.

Particularly interesting from a physical point of view is the behaviour of model D, with  $\tau_D \ll \tau_A$ . As  $\eta$  is large, the magnetic field is unable to contain the mountain at the magnetic pole. Consequently, the plasma slips through the field and falls towards the magnetic equator, where it is reflected at the boundary; that is, the mountain meets its counterpart centred at the other pole. As a result,  $\epsilon$  oscillates around the abscissa. A realistic neutron star never enters the regime  $\tau_D \ll \tau_A$ , but the tendency of the mountain to slip and bounce affects the dynamics for all values of  $\tau_D/\tau_A$ , as discussed in section 3.3.

Fig. 2 shows the density contours (dashed curves) and projected magnetic flux surfaces (solid curves) for a meridional slice of model C. Snapshots are taken at  $t/\tau_A = 0, 0.428, 1.09, 1.76, 4.76, 5.80$ . At  $t/\tau_A = 0.428$  and  $1.76$ ,  $\epsilon$  is in decline, according to Fig. 1 (model C, dashed line). At



**Figure 2.** Meridional section of model C at  $t/\tau_A = 0, 0.428, 1.09, 1.76, 4.76, 5.80$  (top left to bottom right). Shown are density contours (dashed curves) with values  $\log_{10}(\rho/\rho_0) = -13, -12, -11, -10.7, -10.5, -10.3$  and magnetic flux surfaces in cross-section (solid curves). The plasma diffuses through the flux surfaces while the magnetic field relaxes radially.

$t/\tau_A = 0, 1.09$  and  $4.76$ ,  $\epsilon$  is in a plateau. The configuration settles down at  $t = 5.80\tau_A$ .

The oscillations in Fig. 1 and Fig. 2 are driven by the hydrostatic pressure gradient perpendicular to the magnetic flux surfaces. Their amplitude remains bounded. Pressure-driven instabilities, such as the interchange or ballooning mode, grow when the field line curvature has a component along the pressure gradient (i.e.  $\kappa \cdot \nabla p > 0$ , where  $\kappa = \mathbf{b} \cdot \nabla \mathbf{b}$  and  $\mathbf{b} = \mathbf{B}/B$ ), a configuration termed unfavourable curvature (Lifschitz 1989). The top left panel of Fig. 2 shows clearly that the pressure gradient (which is proportional to the density gradient) in the ideal-MHD equilibrium is opposed to the curvature, preventing the onset of a pressure-driven instability. Line tying also contributes to stability (VM08).

### 3.2 Nonaxisymmetric dynamics

The stability of an MHD system changes considerably upon passing from two to three dimensions. It turns out that, in the ideal case, the additional degree of freedom accommodates toroidal Parker modes that rearrange the axisymmetric equilibrium into a slightly nonaxisymmetric state (VM08). The stability of this state when resistivity is switched on is the concern of this section. The relevant models are labelled E–H in table 1.

Following section 3.1, we first examine the time evolu-

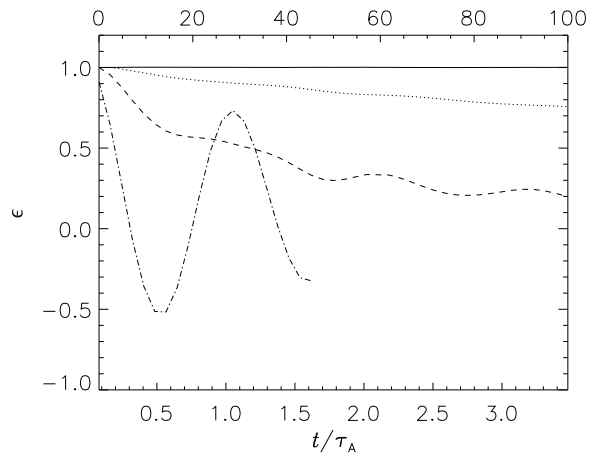


**Figure 3.** Evolution of mass ellipticity  $\epsilon$  for different Lundquist numbers (from top to bottom)  $Lu = 2.99 \times 10^{14}, 4.25 \times 10^3, 4.25 \times 10^2, 42.5$  (solid, dotted, dashed, dash-dotted) for the nonaxisymmetric models E–H with  $M_a = M_c$ . The time is measured in units of the Alfvén time (bottom axis). The top axis measures the time in units of the diffusion time for model G. As in Fig. 1,  $\epsilon$  decays on the diffusive time-scale.

tion of  $\epsilon$  for models E–H. The results are summarized in Fig. 3. Strictly speaking, the definition of  $\epsilon$  is only meaningful for an axisymmetric configuration. However, the three-



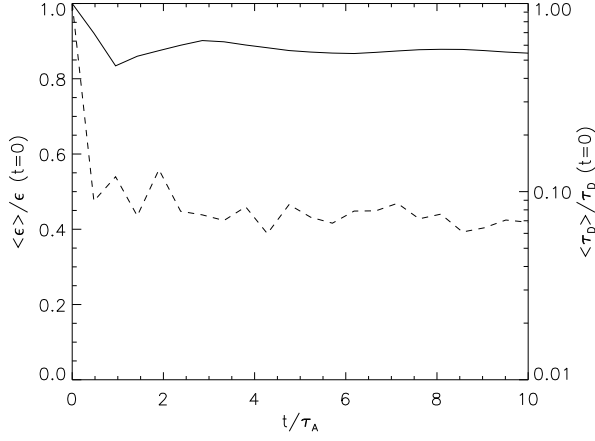


**Figure 5.** Mass ellipticity  $\epsilon$  (solid curve, left linear axis) and diffusion time-scale  $\tau_D$  (dashed curve, right logarithmic axis) as functions of time, in units of the Alfvén time, for model A. Both quantities are normalized to their initial values. During the first cycle,  $\tau_D$  drops by 91 per cent.

dimensional equilibrium deviates from axisymmetry by less than 0.8 per cent (VM08), so  $\epsilon$  is a good proxy for the global hydromagnetic structure. We find that Model E is stable for  $t \leq 3.5\tau_A$ . In models F and G, which have  $Lu \lesssim 4.25 \times 10^3$  and  $\tau_A = 124\tau_0$ , the mountain dissipates on the diffusive time-scale (e.g.  $\tau_D = 5.26\tau_0$  for model G). Model H ( $Lu = 42.5$ ) exhibits the pressure-driven oscillations observed in model D (cf. Fig. 1).

The three-dimensional hydromagnetic structure of model G is captured in a series of snapshots in Fig. 4. Shown is the mountain (orange surface), delineated by the isosurface  $\rho = 1.03 \times 10^9 \text{ g cm}^{-3}$ , along with the magnetic field lines (blue and green curves), at the instants  $t/\tau_A = 0, 1.70, 3.40, 5.09, 6.79, 8.57$ . The initial configuration (top-left panel) is the outcome of the three-dimensional undulating submode of the Parker instability (VM08). The field lines curve towards the magnetic poles, while the orange isosurface spreads equatorwards by 32 per cent relative to its initial position. Soon after the resistivity is switched on (top-middle panel), the system behaves like model C: magnetic tension straightens the field lines radially, while the plasma slips laterally through the flux surfaces, allowing the magnetic mountain to escape its polar confinement and spread over the neutron star surface. However, the non-axisymmetric configuration is the saturation state of the transient Parker instability. Hence, unlike model C, the global hydromagnetic oscillations in model G have already died away. The instability time-scale is given by the diffusion time-scale, not the tearing-mode time-scale  $(\tau_D \tau_A)^{1/2}$  (Furth et al. 1963).

### 3.3 Oscillation enhanced diffusion

As the axisymmetric mountain oscillates laterally, the field gradients steepen whenever the field compresses. This effect accelerates resistive relaxation. Fig. 5 plots  $\tau_D$  (right, logarithmic axis) and  $\epsilon$  (left, linear axis) as functions of time for model A. During the first cycle,  $\tau_D$  drops to nine per cent

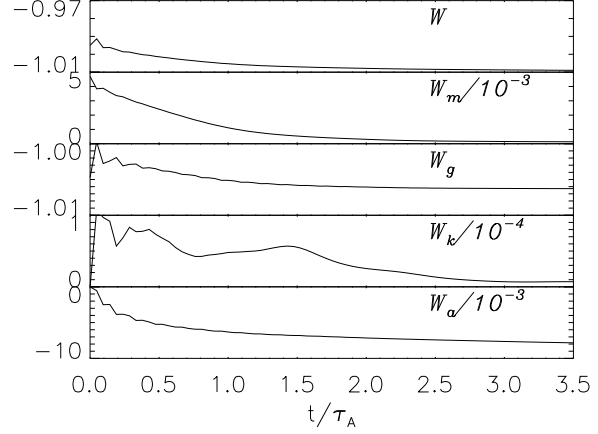


**Figure 6.** Temporal evolution of the total, magnetic, gravitational, kinetic, and acoustic energies  $W$ ,  $W_m$ ,  $W_g$ ,  $W_k$ , and  $W_a$  (top to bottom) for model C, all normalised to  $W_0 = 2.4 \times 10^{36}$  erg and corrected for mass loss through the outer border. Note the decrease in  $W_m$  due to magnetic dissipation.

of its original value and diffusion proceeds proportionally faster. The effect of diffusion is two-fold. (i) The plasma slips through magnetic flux surfaces and moves towards the magnetic equator. Eventually, as seen in the lower middle panel in Fig. 2, it covers the surface evenly and  $\epsilon$  decreases (Fig. 1). (ii) Magnetic tension causes the field lines to straighten radially. Close to the magnetic equator, the hydrostatic pressure from the drained plasma also drives the magnetic field outwards.

Mouschovias (1974) showed that an isothermal gravitating MHD system possesses a total energy  $W$ , which can be written as the sum of gravitational ( $W_g$ ), kinetic ( $W_k$ ), magnetic ( $W_m$ ), and acoustic ( $W_a$ ) contributions, defined by Eqs. (10)–(13) in VM08. In ideal MHD,  $W$  is a conserved quantity. Adding resistivity allows the magnetic flux to dissipate, converting  $W_m$  to  $W_a$  via a source term  $(\gamma - 1)\eta|j|^2$  in the energy equation, where  $\gamma$  is the adiabatic index. In an isothermal setup, this source term vanishes and the energy equation is trivially satisfied; heat is absorbed by a reservoir.

The time dependence of the above four contributions to the energy integral for the axisymmetric model C are shown in Fig. 6. Following VM08, we correct for mass loss through the  $r = R_m$  border by multiplying  $W_g$ ,  $W_k$ , and  $W_a$  by  $M(t=0)/M(t)$ , where  $M(t)$  is the total mass in the simulation volume at time  $t$ . Clearly, some energy is converted to heat:  $W$  drops by 1.4 per cent during the interval  $t \lesssim 3\tau_A$ , as the magnetic field dissipates.  $W_g$  decreases because the accreted matter, which is initially confined at the magnetic pole, distributes itself evenly over the star’s surface.  $W_k$  rises sharply when the whole system reconfigures and then slowly decreases due to numerical dissipation.  $W_a$  decreases along with  $|\nabla p|$ .

Fig. 7 shows the time dependence of the different energy contributions for the nonaxisymmetric model G. Similar to Fig. 6,  $W$  drops by  $\approx 2$  per cent on the diffusion time-scale. The main losses occur in  $W_m$ , which drops by one order of magnitude, and  $W_g$ , which decreases by 1 per cent (from a high base). The kinetic energy slowly rises, as an

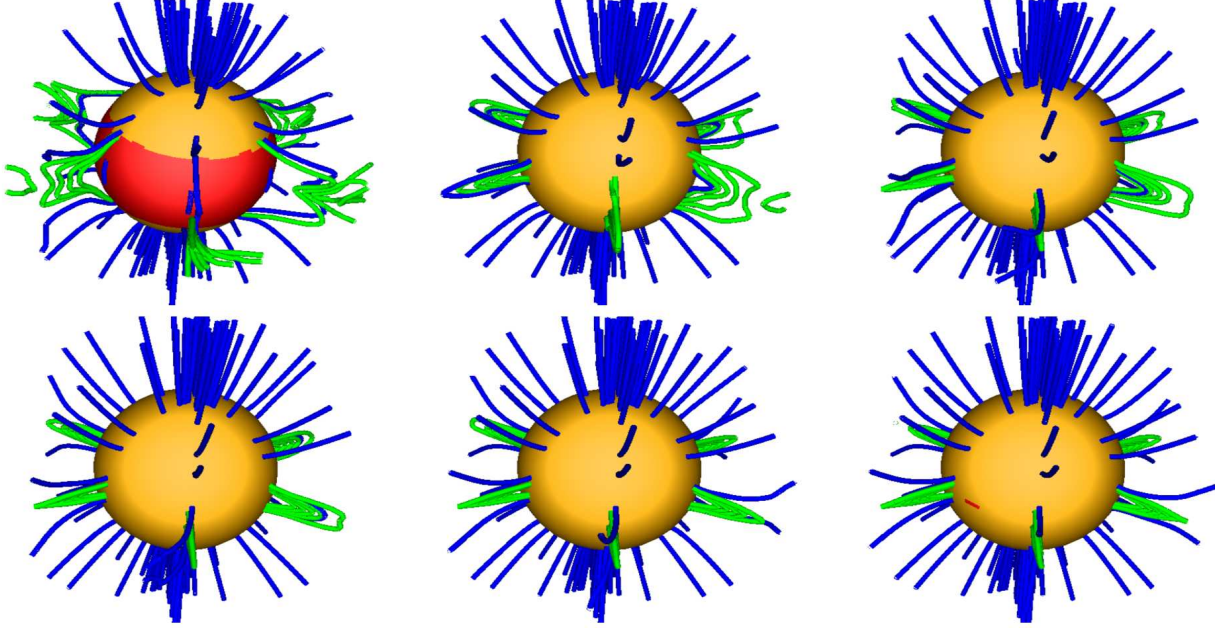


**Figure 4.** Density and magnetic field structure of model G at  $\tau/\tau_A = 0, 1.70, 3.40, 5.09, 6.79, 8.57$  (from top left to bottom right). The mountain (orange surface) is defined by the isosurface  $\rho(r, \theta, \phi) = 1.03 \times 10^9 \text{ g cm}^{-3}$ . In order to assist with visualization, all length-scales of the mountain and the field lines are magnified five-fold. The footpoints of the blue field lines start from the stellar surface, while green field lines start from the equatorial plane.

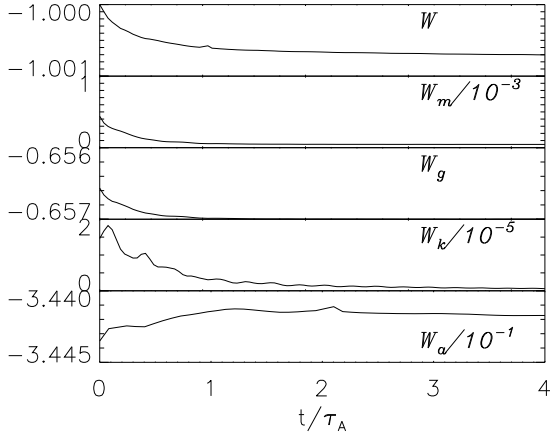


**Figure 7.** The evolution of total, magnetic, gravitational, kinetic, and acoustic energies  $W$ ,  $W_m$ ,  $W_g$ ,  $W_k$ , and  $W_a$  (top to bottom) for model G, all normalised to  $W_0 = 2.1 \times 10^{36} \text{ erg}$ , as a function of time (in units of the Alfvén time) and corrected for mass loss through the outer border.

overstable mode grows (see section 6.2). Since ZEUS-MP does not explicitly include viscosity,  $W_k$  dissipates numerically (i.e. through the grid viscosity).

On the other hand, discretizing the continuous MHD equations introduces numerical errors that dissipate magnetic energy and can damp the growth of unstable modes. This numerical viscosity,  $\nu$ , can therefore artificially stabilize our configuration. A good measure for the relative importance of  $\nu$  is the magnetic Prandtl number,  $Pr_m = \tau_D/\tau_{\text{visc}}$ , where  $\tau_{\text{visc}} = \rho l_v^2/\nu$  with  $l_v$  being a characteristic length scale for velocity gradients and  $\nu$  the viscosity. Since  $\nu$

owes its existence to the discretization of the MHD equations, it depends on the grid size and the field gradients. In order to obtain an accurate estimate for  $Pr_m$ , we compute the timescale,  $\tau_{\text{visc}}$ , on which ideal-MHD oscillations of an axisymmetric configuration die away (Payne & Melatos 2006) and compare it to the diffusive timescale,  $\tau_D$ , finding  $Pr_m = 1.03 Lu$ . Hence, the contribution of numerical viscosity is generally small (e.g.  $Pr_m \approx 10^{-3} \ll 1$  in model D).

## 4 MAGNETIC FIELD STRUCTURE

The global hydromagnetic evolution observed in section 3 occurs on the ohmic time-scale. This indicates that relaxation is dictated by magnetic diffusion rather than resistive transient instabilities on short time-scales, such as the large-scale tearing mode or the localized gravitational mode (Furth et al. 1963). Transient instabilities occur in the neighbourhood of current sheets, which dissolve into magnetic islands and dissipate. In this section, we examine the magnetic geometry of the resistively relaxing mountain to check whether it is consistent with the above view that diffusion on large scales dominates the evolution.

### 4.1 Neutral surfaces

We begin by investigating the magnetic field structure of the axisymmetric model C (Fig. 2). The initial equilibrium configuration is depicted in the top-left panel. Notice that there are no magnetic neutral points present. The mountain is held in place by the tension of the line-tied magnetic field.

Does the configuration contain current sheets? Hanasz et al. (2002) showed that the undulating submode

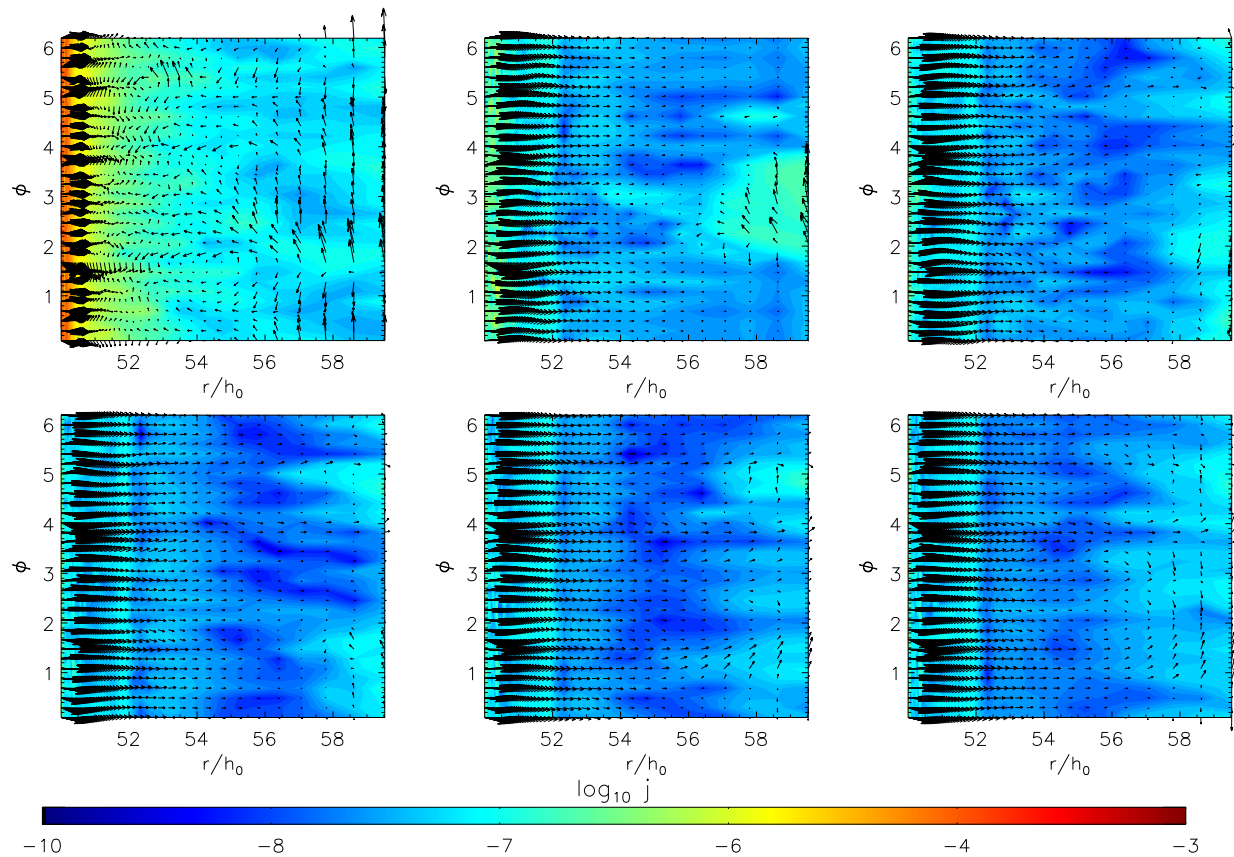


**Figure 8.** Equatorial slices of the magnetic structure and current flows in model G at  $t/\tau_A = 0, 1.69, 3.39, 5.08, 6.77, 8.55$  (from top left to bottom right). Shown are the projections of the magnetic field vectors onto the plane  $\theta = 1.5$  rad (arrows) and the modulus of the current density  $|j|$  (color coded).

of the Parker instability in a Cartesian geometry creates current sheets in the plane perpendicular to the magnetic flux surfaces between regions with alternating polarity. Fig. 8 displays a time series of equatorial slices of the magnetic field from model G at  $t/\tau_A = 0, 1.69, 3.39, 5.08, 6.77, 8.55$ . The projection of  $\mathbf{B}/B$  onto the equatorial plane is indicated by arrows, while the current density  $|j|$  is color coded. The top left panel shows the initial configuration for our experiment, generated from an axisymmetric mountain after the undulating submode of the Parker instability saturates. While  $|j|$  is greatest close to the stellar surface, where  $B$  is high, long radial current filaments are also clearly present, albeit not as distinctly as in Hanasz et al. (2002). The filaments are neutral sheets.

## 4.2 Reconnection

Reconnection occurs at the current sheets in Fig. 8, quickly smoothing the toroidal gradients. Line tying at the stellar surface forces the field lines to adjust into a dipolar configuration. A finite resistivity therefore acts to restore axisymmetry. In addition, the line-tying boundary condition acts as a source of magnetic flux, which is thence transported radially outward by diffusion.

Where does reconnection occur? Schindler et al. (1988) pointed out that a necessary and sufficient condition for

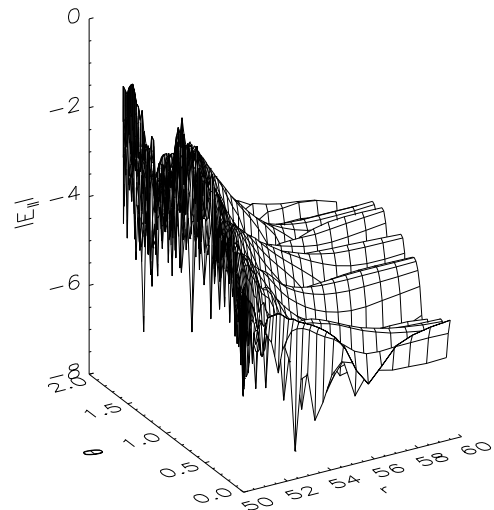


**Figure 9.** Meridional slice of the local field-aligned electric field  $\log_{10} |\mathbf{E} \cdot \mathbf{B}|$ , normalised to  $B_0 E_0 = 1.51 \times 10^{-11} B_0 h_0^{-1}$  for model G. Reconnection mainly occurs near the stellar surface in the magnetic belt but also in the outer equatorial region (at  $r \gtrsim 56 h_0$  and  $0.7 \lesssim \theta \lesssim 1.5$ ).



global magnetic reconnection along some field line  $C$  is that the electric field has a component parallel to  $\mathbf{B}$ ,

$$\int_C ds \mathbf{E} \cdot \mathbf{B} \neq 0, \quad (1)$$

where the integral is taken along  $C$ . (Equivalently, the helicity changes with time.) We plot a meridional slice of  $\mathbf{E} \cdot \mathbf{B}$  at  $\phi = 2.3$  rad in Fig. 9. Not surprisingly,  $\mathbf{E} \cdot \mathbf{B}$  is highest in the magnetic belt region, close to the star's surface. However, the undulating submode of the Parker instability also induces small toroidal currents (top left panel in Fig. 8), so that  $\mathbf{E} \cdot \mathbf{B}$  is high in the equatorial region too. We integrate  $\mathbf{E} \cdot \mathbf{B}$  along two sample field lines with footpoints at  $(\tilde{x}_0, \theta_0, \phi_0) = (0, 0.2, 4.03)$  (field line ①) and  $(0, 1.0, 4.03)$  (field line ②) and find  $\int_C \mathbf{E} \cdot \mathbf{B} = -8.6 \times 10^{-14} B_0$  (field line ①) and  $\int_C \mathbf{E} \cdot \mathbf{B} = -3.2 \times 10^{-16} B_0$  (field line ②) respectively. The topology of the magnetic field is discussed in section 4.3, where we show that field line ① undergoes reconnection while field line ② does not.

### 4.3 Topology

In this subsection, we briefly discuss the change in magnetic topology brought about by reconnection. Fig. 10 displays the magnetic field lines (solid curves) in three meridional slices  $\phi = 0, 1.96, 3.93$  (left, middle, right columns) for model G. One immediately notices that there is a Y-point located at  $(r, \theta) \approx (56h_0, 1.4 \text{ rad})$  in the top-left panel of the figure. The Y-point owes its existence to a boundary effect in the ideal-MHD simulation: during the onset of the Parker instability, the plasma is pushed out of the integration volume through the outer boundary. The subsequent backflow topologically separates the previously connected field lines.

Associated with the Y-point is a current sheet at  $\theta \approx 1.4$  rad, which meanders like a band in the  $\phi$  direction. A current sheet naturally triggers reconnection. The bottom row of Fig. 10 shows the same slices as the top row after  $0.6\tau_D$ . Indeed, the field lines have reconnected: they are not topologically separated anymore, and the current sheet has vanished. Alternatively, it is conceivable that the current sheet moves along with the plasma flow from its initial position at  $\theta = 1.4$  to the upper boundary at  $\theta = \pi/2$ .

The concept of rational magnetic surfaces, where the field lines close upon themselves, plays an important role in a local plasma stability analysis (Lifschitz 1989). The bending of field lines as a result of a Lagrangian displacement  $\boldsymbol{\xi}$  is associated with an increase in potential energy, given by  $\mathbf{B} \cdot \nabla \boldsymbol{\xi}$ . In a tokamak geometry, it can be shown that this term vanishes on a rational surface, which is directly related to the pitch angle  $B_\phi/B_p$ : the safety factor is defined as  $q = dB_\phi/dB_p$ , and a rational surface is one where  $q$  is a rational number. In Fig. 11, we plot the pitch angle as a function of the arc-length coordinate  $\eta$  (right panels) for four different field lines (labelled ①–④ in the left panel) in model G. Close to the pole (lines ①–③), the pitch angle stays below  $\approx 3$  per cent. For line ④, it increases towards the equator, ultimately reaching  $\approx 20$  per cent. The zero crossing for ④ indicates that  $B_\phi$  changes sign, a relic of the undulating submode of the Parker instability which gives birth to this state. Diffusion does not eliminate the toroidal component completely.

We attempted for completeness to characterize the magnetic topology near the neutral surface using scale invariants of the strain tensor  $\partial B_i/\partial x_j$  (Chong et al. 1990; Parnell et al. 1996; Peralta et al. 2008), but this approach yields ambiguous results in this instance.

## 5 RELAXATION TIME

We are now in a position to compute how long it takes for a magnetically confined mountain to relax resistively, given  $\eta$  and  $M_a$ . Ultimately, as  $t \rightarrow \infty$ , the mountain spreads itself uniformly over the stellar surface [i.e.  $\rho = \rho(r)$ ], threaded by a dipole field (i.e.  $j = 0$  everywhere). However, this process does not approach completion for realistic  $\eta$  over the lifetime of an accreting neutron star.

Let us define the ohmic relaxation time to be the time that elapses before the mountain relaxes to  $e^{-1}$  its initial ellipticity. Fig. 1 presents  $\epsilon(t)$  for an axisymmetric mountain with  $M_a = M_c$  as a function of the conductivity  $\sigma = \eta^{-1}$ . Reading off  $\tau_1$  from  $\epsilon(\tau_1) = e^{-1}\epsilon(0)$ , and fitting the trend by linear least squares, we obtain

$$\frac{\tau_1}{\tau_0} = 1.7 \times 10^{-3} \sigma, \quad (2)$$

where  $\sigma$  is measured in units of  $\sigma_0 = \eta_0^{-1} = 1.86 \times 10^6 \text{ s}^{-1}$ . For the upscaled star with a realistic  $\eta_r$  we find  $\tau_1 = 6.3 \times 10^6 \text{ yr}$ , which is comparable to the fiducial accretion time-scale  $\tau_{\text{acc}} = 10^6 - 10^7 \text{ yr}$ .

Fig. 3 presents  $\epsilon(t)$  for a nonaxisymmetric mountain with  $M_a = M_c$ . Applying the same procedure from the previous paragraph to Fig. 3, we find

$$\frac{\tau_1}{\tau_0} = 0.02\sigma. \quad (3)$$

For an upscaled neutron star with realistic  $\eta_r$ , we find  $\tau_1 = 7.6 \times 10^7 \text{ yr}$ , comparable to the fiducial accretion time-scale. Astrophysically, this is the key result of this paper: magnetic mountains in three dimensions relax resistively over  $\sim 10^5 - 10^8 \text{ yr}$ , (depending on the particular value of  $\sigma$ ; see section 2.3), not over shorter time-scales like  $\tau_A$  and  $(\tau_A \tau_D)^{1/2}$ . Note that  $\tau_D$  is a local quantity for a stationary mountain;  $\tau_1$  is a better measure of the global diffusion time.

We compare  $\tau_1$  to the growth time of the resistive Parker instability, whose dispersion relation is calculated in appendix B. The growth time is shortest for short-wavelength modes and is therefore set by the grid scale ( $k \approx 6.6h_0^{-1}$ ) in our units. Also, the ratio of magnetic pressure to gas pressure,  $\alpha$ , is maximal in the magnetic belt region, where the magnetic pressure balances the gas pressure, viz.  $\alpha \approx 1$ . The growth rate is independent of  $k$  and is given by  $\Gamma = [1/2(1 - 2\alpha^2)[\alpha/(1 + \alpha)](g^2/k^2 u^2)(1/\tau_D)$ , where  $\tau_D$  is the time required to diffuse over one scale height. Applying equation (B17) to the axisymmetric model C, we find the Parker growth-rate to be  $\Gamma = 4.07 \times 10^6 \tau_0^{-1}$ . Fig. 1 shows clearly that  $\tau_1 \gg \Gamma^{-1}$ , further supporting our conclusion that the resistive relaxation occurs on the diffusion time-scale and does not involve MHD instabilities. The same conclusion applies for the nonaxisymmetric model G, with the same growth rate as for the axisymmetric model.

Another way to present the results on  $\tau_1$  is to ask how  $\epsilon$  varies with the accretion rate  $\dot{M}$ . The simulations underlying Fig. 12 differ from the others in this paper in one



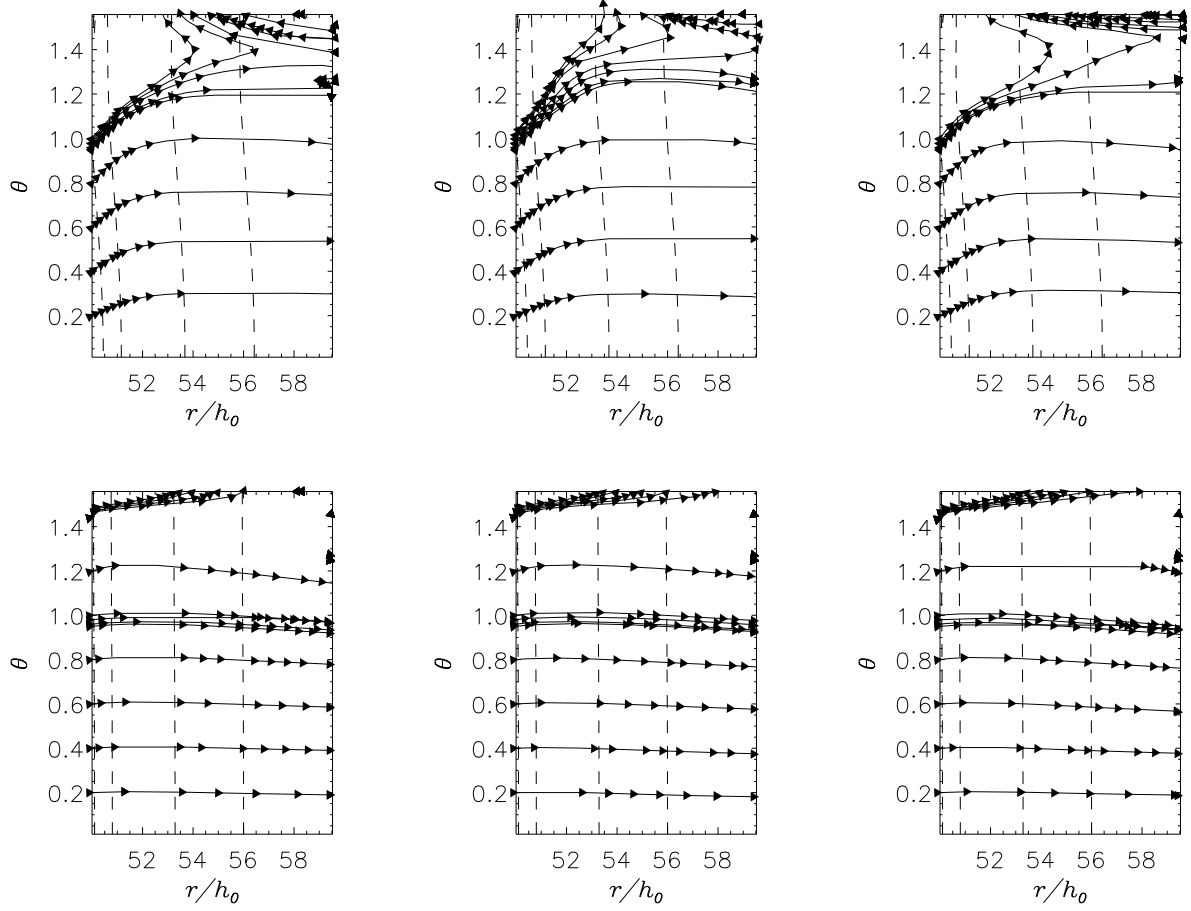


**Figure 10.** Density contours (dashed) and magnetic field lines (solid) for meridional slices at  $\phi = 0, 1.96, 3.93$  rad (left to right columns) and  $t/\tau_D = 0, 201$  (top and bottom row) for model G. The direction of the magnetic field is indicated by arrows. At the Y-point in the top-right corner of each panel, reconnection occurs.

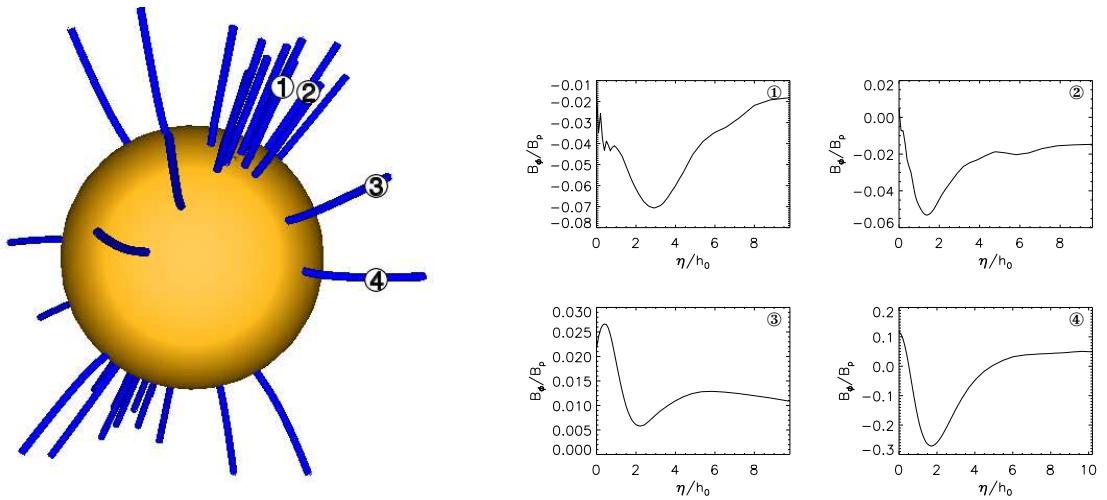


**Figure 11.** Magnetic pitch angle  $B_\phi/B_p$  (right panel) as a function of arc length  $\eta$  along four magnetic field lines ①–④ for model G, for a snapshot taken at  $t = 0.6\tau_D$ . Field lines (blue curves) are identified in the left panel. The mountain is defined by the orange isosurface  $\rho(r, \theta, \phi) = 1.04 \times 10^9 \text{ g cm}^{-3}$ . Red indicates the neutron star surface  $r = R_*$ . In order to help visualize the structure, all length scales of the mountain and the field lines are magnified five-fold.

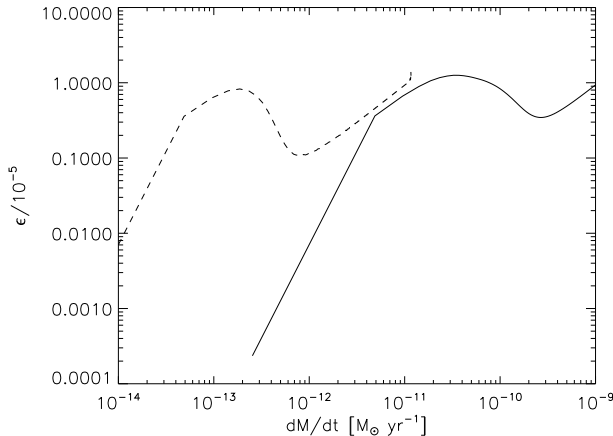


**Figure 12.** Mass ellipticity  $\epsilon$  versus accretion rate  $\dot{M}$  (in units of  $10^{-4} M_{\odot} \text{ yr}^{-1}$ ) for an axisymmetric grown mountain [see text and Vigeliu & Melatos (2008b)]. The solid (dashed) curve represents a mountain aged  $t = 10^6$  yr ( $t = 10^8$  yr). Although  $\epsilon$  is generally higher for the older mountain, since more mass has been accreted, it almost touches the curve for the younger mountain, because the resistive instability acts to reduce  $\epsilon$ .

important respect: the mountain is grown from scratch over time (starting from  $M_a = 0$ ), with mass injected at the poles of an initially dipolar magnetic field, at a rate  $\dot{M}$  and with  $\eta \neq 0$  throughout the experiment. In other words, resistive relaxation *competes simultaneously* with accretion. By contrast, in Figs. 1–11, a Grad-Shafranov equilibrium is imported into ZEUS-MP,  $\eta$  is switched on at  $t = 0$ , and the mountain subsequently relaxes. Growing the mountain confers several advantages: it reflects the astrophysical process of burial more faithfully and enables us to reach  $M_a = 10 M_c$ , cf.  $M_a \leq 1.4 M_c$  with the Grad-Shafranov method. The disadvantage is that, at present, we cannot study how the mountain relaxes after accretion stops, because ZEUS-MP fails when the injection “nozzles” are turned off (suddenly or with taper), due to a numerical instability (the grown mountain contains nonzero flows). We are therefore unable to compare the two numerical experiments exactly, although they are in close qualitative agreement. A detailed explanation of the injection algorithm and verification tests can be found in Vigeliu & Melatos (2008b).

A crucial question is whether the Grad-Shafranov equilibria can be uniquely attained as accretion onto the magnetic poles occurs, in particular, when  $\eta \neq 0$ . The experiments conducted by growing the mountain ab initio [Fig. 12 and Vigeliu & Melatos (2008b); Vigeliu (2008)] mimic time-dependent accretion more faithfully. The infalling plasma continuously deforms an initially dipolar field and every snapshot represents the equilibrium configuration for a particular  $M_a$ . These equilibria are in good agreement with previous results obtained analytically or numerically with the Grad-Shafranov code [cf. Fig. 4.11 in Vigeliu & Melatos (2008b)]. In particular, we find no evidence for (ideal or resistive) instabilities occurring in the low- $M_a$  regime.

On the other hand, the unavoidably finite size of the simulation box leads to a subtle uniqueness problem. The material that is added to the pole pushes the field lines to-

wards the equator. Because of the boundary conditions we use, these field lines jump discontinuously when they touch the bottom right-hand corner of the box from  $\partial_r \mathbf{B} = 0$  when penetrating the boundary  $r = R_m$  to  $B_r = 0$  when penetrating the boundary  $\theta = \pi/2$  (compare the top-right corner of the top-right and bottom-left panels in Fig. 10). In effect, this is a “reconnection-type” event which changes the topology of the field lines, their connectivity to the “outside world”, and therefore the effective functional form of  $dM/d\psi$  (which we assume to be constant throughout the run). In practice, it is likely the effect is very small, the evidence being (i) the small mass outflow ( $\lesssim 1$  per cent of the total mass) through  $r = R_m$  during a typical run, and (ii) the very similar equilibria obtained from solving the Grad-Shafranov equation and growing the mountain ab initio (Vigeliu & Melatos 2008b). In principle, though, it can lead to different final states if the mountain is grown with and without resistivity turned on<sup>1</sup>.

Fig. 12 displays the ellipticity as a function of  $\dot{M}$  for a young ( $t = 10^6$  yr, solid curve) and an old ( $t = 10^8$  yr, dashed curve) object. To perform the simulation over a practical length of time, we artificially increase  $\eta$  to  $10^{13.85} \eta_r$  (solid curve) and  $10^{15.85} \eta_r$  (dashed curve). We then use the scaling  $\tau_1 \propto \eta^{-1}$  derived from Figs. 1 and 3 to relate the results to astrophysical time-scales. We point out that each curve in Fig. 12 basically displays  $\epsilon(t)$  and we can relabel the abscissa using  $M_a = \dot{M}t$ .

There are two opposing effects in the figure. First, the older object has generally higher  $\epsilon$  for a given  $\dot{M}$ , simply because  $M_a$  is higher. Second, resistive relaxation has more time to reduce  $\epsilon$  in the older object, so the two curves almost touch at  $\dot{M} \approx 5 \times 10^{-8} M_{\odot} \text{ yr}^{-1}$ . The injection algorithm induces global hydromagnetic perturbations; these numerical artifacts are visible as oscillations at the high- $\dot{M}$  end of either curve.

How does our relaxation time compare to previous estimates? In the small- $M_a$  regime, Melatos & Payne (2005) found analytically that resistive relaxation stalls mountain growth at  $\epsilon \sim 10^{-5}$  (assuming electron-phonon scattering with a crustal temperature of  $T = 10^8$  K). Our results suggest that a mountain with  $M_a = M_c = 1.2 \times 10^{-4} M_{\odot}$  relaxes resistively over  $\sim 10^5 - 10^8$  yr. Furthermore, when accretion and relaxation proceed together, we find again that  $\epsilon$  saturates at  $\sim 10^{-5}$ , even for  $M_a > M_c$ , in accord with Melatos & Payne (2005).

Similar estimates were given by Brown & Bildsten (1998) who evaluated the diffusion time in the crust. Taking into account electron-phonon and electron-impurity scattering, they found that phonon scattering dominates impurity scattering (provided  $Q \lesssim 1$ ) and  $\tau_D \sim 10^4$  yr when the star accretes at the Eddington rate. However, these authors considered only spherically symmetric accretion and disregarded the global magnetic structure. Cumming et al. (2004) found  $\tau_D \sim 10^8$  yr for a crustal temperature of  $T = 10^6$  K, in accord with our results.

We conclude this subsection with a brief discussion of how the relaxation time changes with  $M_a$ . Fig. 13 compares  $\epsilon$  for two axisymmetric models with different accreted masses,  $M_a = 0.6 M_c$  (solid curve) and  $M_a = 1.4 M_c$  (dashed curve),

<sup>1</sup> Sterl Phinney, private communication

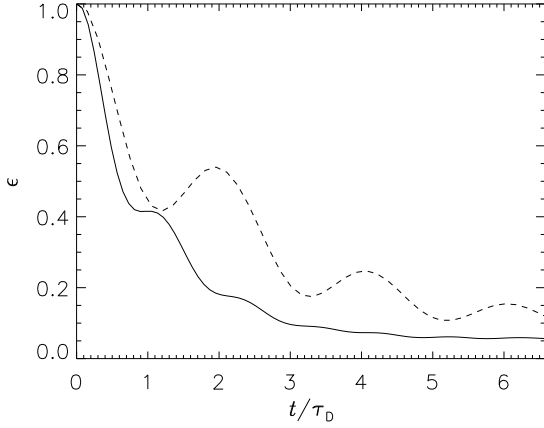


**Figure 13.** Evolution of mass ellipticity  $\epsilon$  as a function of time in units of the respective diffusion times  $\tau_D$  for axisymmetric models with  $M_a = 0.6M_c$  (solid curve) and  $M_a = 1.4M_c$  (dashed curve). The Lundquist number for both models is  $Lu = 1$ . The diffusion time is  $\tau_D = 123\tau_0$  ( $\tau_D = 66.4\tau_0$ ) for  $M_a = 0.6M_c$  ( $M_a = 1.4M_c$ ).

but the same Lundquist number  $Lu = 1$ . Note that  $\epsilon$  is displayed as a function of time in units of the respective diffusion time,  $\tau_D = 123\tau_0$  ( $\tau_D = 66.4\tau_0$ ) for  $M_a = 0.6M_c$  ( $M_a = 1.4M_c$ ). The magnetic field of the  $M_a = 1.4M_c$  model is more distorted and, consequently,  $\tau_D$  is shorter. Both models exhibit resistive relaxation on the diffusion time-scale.

## 6 REEMERGENCE OF THE BURIED MAGNETIC FIELD

### 6.1 Magnetic dipole moment

An important diagnostic of the global magnetic structure is its magnetic dipole moment. This integrated value has the advantage that it is observationally accessible (van den Heuvel & Bitzaraki 1995). Indeed, the observed reduction of the magnetic dipole moment by accretion is a key motivation of the magnetic mountain concept (PM04).

Following VM08, we define the magnetic multipole moment tensor as

$$d_{ij}(r) = r^{i+1} \int d\Omega Y_{ij}^* \mathbf{r} \cdot \mathbf{B}, \quad (4)$$

where  $Y_{ij}$  denotes the spherical harmonics and  $\mathbf{r}$  is the position vector. Henceforth, we evaluate  $d_{ij}$  at the simulation boundary  $r = R_m$  and drop  $r$ .

The evolution of  $d_{10}$ , plotted in Fig. 14, illustrates the effect of ohmic diffusion on the magnetic structure. Initially,  $d_{10}$  is buried by the distorted magnetic field. The resistive instability then allows  $\mathbf{B}$  to straighten radially and reduce the field line curvature (cf. bottom-middle panel in Fig. 2), as described in section 3.1. Ultimately, the line-tying condition of the inner boundary forces  $d_{10}$  to approach the underlying dipole moment of the star before accretion, as the screening currents in the mountain dissipate. In this sense, one can say that the buried magnetic field reemerges.

The physical mechanism behind reemergence is illuminated by examining the radial dependence of the dipole moment, snapshots of which are plotted in Fig. 15, plotted at

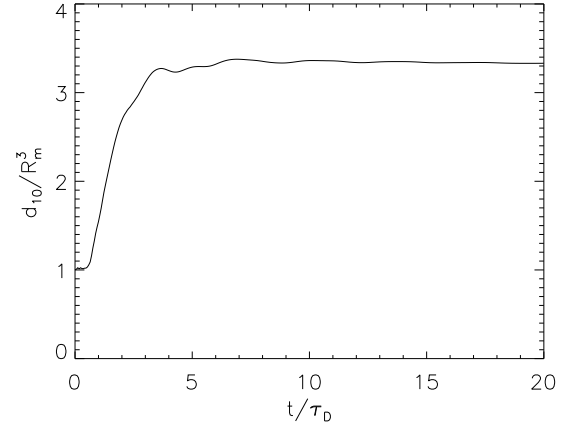


**Figure 14.** Normalized magnetic dipole moment  $d_{10}/R_m^3$  versus time (in units of the diffusion time) for model C. The resistive instability relaxes the magnetic field radially, such that  $d_{10}$  peaks at  $t = 7\tau_D$ . Eventually, the screening currents in the mountain dissipate and  $d_{10}$  tends to its initial value.

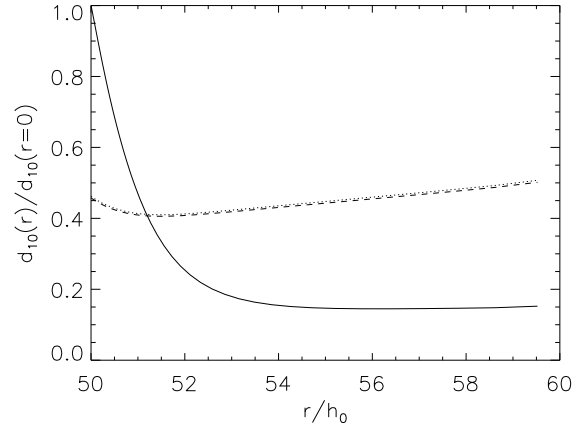


**Figure 15.** Magnetic dipole moment  $d_{10}(r)$  [normalised to  $d_{10}(r = 0)$ ] versus radius (in units of  $h_0$ ) for model C at times  $t/\tau_D = 0, 333, 665$  (solid, dotted, dashed curves).

$t/\tau_D = 0, 333, 665$  (solid, dotted, and dashed curves, respectively). Initially,  $d_{10}$  is screened within a thin layer near the surface. As the screening currents dissipate resistively, magnetic flux is transported radially outward, thereby increasing the dipole moment measured by an outside observer.

The nonvanishing components of the magnetic dipole and quadrupole tensors are displayed in Fig. 16 for a non-axisymmetric mountain (model G). As for the axisymmetric case (Fig. 14),  $d_{10}$  (bottom panel) increases over the diffusion time-scale as the magnetic field relaxes, tending to the underlying value at  $r = R_*$ . Overall,  $d_{10}$  varies by less than 10 per cent over the simulation. The magnetic quadrupole moment  $d_{21}$  approaches zero as diffusion restores the dipolar field.

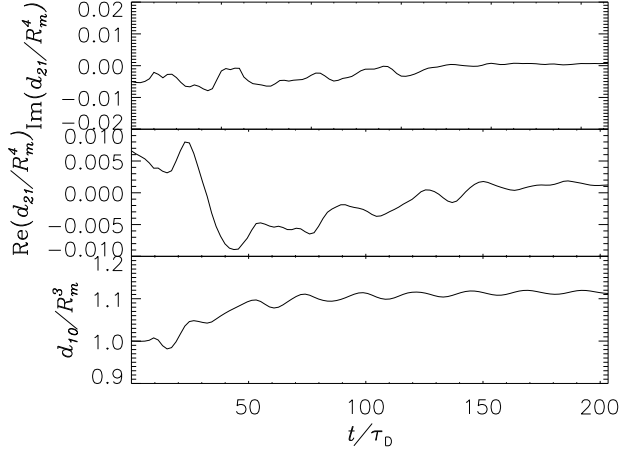


**Figure 16.** Magnetic dipole moment  $d_{10}/R_m^3$  and magnetic quadrupole moment  $d_{21}/R_m^4$  for model G, normalised to the initial value of  $d_{10}/R_m^3 = 7.3 \times 10^{11}$  G, as a function of time (in units of the diffusion time scale  $\tau_D$ ). All other components of the tensor  $d_{ij}$  vanish due to symmetry.

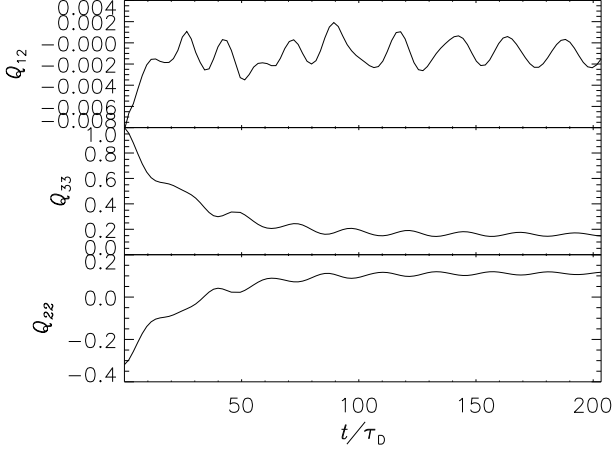


**Figure 17.** Components of the mass quadrupole moment tensor normalised to the maximum of  $Q_{33}$ ,  $7.2 \times 10^{24}$  g cm<sup>2</sup>, as a function of time, in units of the diffusion time-scale, for model G.

## 6.2 Triaxiality

The distorted magnetic field structure in Fig. 2 is accompanied by deformation of the mass distribution. This matters when considering accreting neutron stars as gravitational wave sources. Fig. 17 plots the components of the Cartesian mass quadrupole moment, defined as

$$Q_{ij} = \int d^3x' (3x'_i x'_j - r'^2 \delta_{ij}) \rho(\mathbf{x}'), \quad (5)$$

versus time for the nonaxisymmetric model G. The diagonal elements of  $Q_{ij}$  measure the axisymmetric distortion and are directly related to the ellipticity by  $\epsilon \propto Q_{22} \propto Q_{33}$ . As the mountain relaxes resistively,  $Q_{22}$  and  $Q_{33}$  decrease, asymptoting at  $\sim 20$  per cent of the initial value at  $t \approx 150\tau_D$ . This is normal: plasma diffuses across the flux surfaces and spreads evenly over the stellar surface. However, since magnetic diffusion tends to smooth out gradients in  $\mathbf{B}$ , thereby

reducing the actual diffusion time-scale, we reach an intermediate, metastable state. In this state, the field lines are almost radial but the mountain has not yet diffused to cover the surface evenly. We compute the diffusion time-scale of the metastable state to be  $\tau'_D = 27.6\tau_D$ , five times higher than  $\tau_D = 5.26\tau_D$  of the initial state. Eventually, the remaining plasma diffuses over the time-scale  $\tau'_D$  and  $Q_{ij}$  tends to zero.

The offdiagonal elements of  $Q_{ij}$  (top panels of Fig. 17) measure the deviation from axisymmetry. They decrease on the time-scale  $\tau_1$  and then oscillate around the abscissa. Non-axisymmetric oscillations, observed previously in ideal-MHD calculations (VM08), are excited here when the mountain reconfigures: small numerical inaccuracies perturb the steady-state equilibrium and the mountain readjusts on the Alfvén time-scale. The period is  $\sim 10\tau_D$  for model G. The amplitude initially grows then decays. The existence of such overstable modes is peculiar to a dissipative MHD system. The linear force operator is no longer self-adjoint and its eigenvalues generally have both a real and an imaginary part. The tendency of  $Q_{12}$  to decrease tallies with the observation that resistivity restores axisymmetry by smoothing toroidal gradients, as postulated in section 4.1. It is important to note that the observed oscillations cannot arise if there is a realistic separation between the Alfvén and diffusion timescale. For completeness, we note that the number  $|Q_{11} - Q_{22}| = |Q_{33} + 2Q_{22}|$  is another measure for the departure from axisymmetry. However, it is obvious from Fig. 17 that the magnitude of this number is small compared to the magnitude of the diagonal elements.

## 7 DISCUSSION

The formation of magnetically confined mountains at the poles of an accreting neutron star is one explanation of the observed reduction of the magnetic dipole moment with  $M_a$  in neutron star binaries. Although a magnetic mountain is susceptible to transient, toroidal, ideal-MHD instabilities, these are not disruptive. The saturation state still confines the accreted matter to the magnetic pole, efficiently screening the dipole moment in the long term.

This article is concerned with the fate of a magnetic mountain when a nonzero electrical resistivity switches on. We extend the ideal-MHD code ZEUS-MP to add a resistive term to Ohm's law and perform three-dimensional simulations for different values of the resistivity. In the axisymmetric case, we find that global MHD oscillations compress the magnetic field, accelerating plasma slippage across flux surfaces. As a consequence, the mountain relaxes on a time-scale  $\tau_1$  which is shorter than the diffusion time-scale  $\tau_D$  but comparable to the accretion time-scale. In the nonaxisymmetric case, Ohmic diffusion additionally tends to restore axisymmetry. We do not find any evidence of transient resistive instabilities, like the resistive ballooning mode, on the intermediate tearing mode time-scale  $(\tau_A \tau_D)^{1/2}$ . The mountain persists over  $\sim 10^5 - 10^8$  years, comparable to the duration of the accretion phase in a low-mass X-ray binary (LMXB).

Astrophysically, the key result of the paper can be stated as follows: *magnetically confined mountains in LMXBs are stable (in ideal and nonideal MHD) over the ac-*



cretion time-scale and relax over the typical life-time of radio millisecond pulsars ( $\sim 10^9$  yr) after accretion stops. Jones (2004) argued that the electrical conductivity in the solid crust is significantly lower than that for a homogenous bcc lattice and temperature-independent, with  $\eta = 10^{-24}$  s. For this value, we expect a stationary state at  $M_a \sim 10^{-5} M_\odot$  where the diffusive mass flux escaping the polar cap is exactly replenished by accretion. To study the structure of such a state, and confirm its existence, we must extend the growing simulations in Fig. 12, a key topic for future work.

One shortcoming of the calculations is the neglect of rotation. Accreting millisecond pulsars spin up as fast as  $\Omega \sim 620$  Hz (Galloway 2008). Spitkovsky et al. (2002) found that surface thermonuclear burning is unaffected by rotation in its early stages, but the thermonuclear flame spreads more slowly as time passes. Bhattacharyya & Strohmayer (2007) applied this idea to qualitatively reproduce the light-curves from 4U 1636–536 and SAX J1808.8–3658. The Coriolis force also modifies the continuous part of the ideal-MHD spectrum for axisymmetric configurations with a uniform angular velocity (Hellsten & Spies 1979; Vigelius & Melatos 2008a), especially for short-wavelength modes. However, it does not affect the equilibrium configuration. A simple estimate shows that one requires a transversal speed of  $v \sim 8 \times 10^8$  cm s $^{-1}$  to attain a Coriolis force which is comparable to  $c^2 \nabla P$ . The star may also precess (Chung et al. 2008), complicating the treatment of rotational effects.

Magnetic mountains in LMXBs are promising sources of gravitational waves (Melatos & Payne 2005; Payne & Melatos 2006). For  $M_a \gtrsim 10^{-5} M_\odot$ , there is a fair prospect of detection with next generation interferometric detectors like the Laser Interferometric Gravitational Wave Observatory (LIGO) (VM08). Clearly, the strength of the signal depends critically on the long-term stability of the mountain and the rate at which it relaxes resistively. In a companion paper (Vigelius & Melatos 2008b), we predict the signal-to-noise ratio attainable by LIGO when the resistive results of this paper are included. We also show that the electrical resistivity can be constrained by existing LIGO data, by invoking the Bildsten (1998) torque-balance limit for LMXBs and the Blandford spin-down limit for radio millisecond pulsars (Abbott et al. 2007).

## REFERENCES

- Abbott B., et al., 2007, Phys. Rev. D, 76, 042001  
 Alexiades V., Amiez G., Gremaud P.-A., 1996, Comm. Num. Methods in Engineering, 12, 31  
 Bhattacharyya S., Strohmayer T. E., 2007, ApJ, 666, L85  
 Bildsten L., 1998, ApJ, 501, L89+  
 Biskamp D., 1993, Nonlinear magnetohydrodynamics. Cambridge University Press, Cambridge.  
 Bisnovatyi-Kogan G. S., Komberg B. V., 1974, Soviet Astronomy, 18, 217  
 Brown E. F., Bildsten L., 1998, ApJ, 496, 915  
 Chamel N., Haensel P., 2008, Living Reviews in Relativity, 11  
 Chong M. S., Perry A. E., Cantwell B. J., 1990, Physics of Fluids, 2, 765  
 Chung C. T. Y., Galloway D., Melatos A., 2008, MNRAS (submitted)  
 Cumming A., Arras P., Zweibel E., 2004, ApJ, 609, 999  
 Cumming A., Zweibel E., Bildsten L., 2001, ApJ, 557, 958  
 Fendt C., Čemeljić M., 2002, A&A, 395, 1045  
 Furth H. P., Killeen J., Rosenbluth M. N., 1963, Phys. Fluids, 16, 1054  
 Galloway D., 2008, in 40 Years of Pulsars: Millisecond Pulsars, Magnetars and More Vol. 983 of American Institute of Physics Conference Series, Accreting neutron star spins and the equation of state. pp 510–518  
 Goedbloed J. P. H., Poedts S., 2004, Principles of Magnetohydrodynamics. Cambridge University Press, Cambridge.  
 Haensel P., Zdunik J. L., 1990a, A&A, 229, 117  
 Haensel P., Zdunik J. L., 1990b, A&A, 227, 431  
 Hanasz M., Otmianowska-Mazur K., Lesch H., 2002, A&A, 386, 347  
 Hawley J. F., Stone J. M., 1995, Comp. Phys. Comm., 89, 127  
 Hayes J. C., Norman M. L., Fiedler R. A., Bordner J. O., Li P. S., Clark S. E., ud-Doula A., Mac Low M.-M., 2006, ApJS, 165, 188  
 Hellsten T. A. K., Spies G. O., 1979, Physics of Fluids, 22, 743  
 Jones P. B., 2004, Physical Review Letters, 93, 221101  
 Konar S., Bhattacharya D., 1997, MNRAS, 284, 311  
 Lifschitz A. E., 1989, Magnetohydrodynamics and Spectral Theory. Kluwer Academic Publishers, London.  
 Litwin C., Brown E. F., Rosner R., 2001, ApJ, 553, 788  
 Lovelace R. V. E., Romanova M. M., Bisnovatyi-Kogan G. S., 2005, ApJ, 625, 957  
 Melatos A., Payne D. J. B., 2005, ApJ, 623, 1044  
 Melatos A., Phinney E. S., 2001, Publications of the Astronomical Society of Australia, 18, 421  
 Mignone A., Bodo G., Massaglia S., Matsakos T., Tesileanu O., Zanni C., Ferrari A., 2007, ApJS, 170, 228  
 Mouschovias T. C., 1974, ApJ, 192, 37  
 Parker E. N., 1967, ApJ, 149, 535  
 Parnell C., Smith J., Neukirch T., Priest E., 1996, Phys. Plasmas, 3, 759  
 Payne D. J. B., Melatos A., 2004, MNRAS, 351, 569  
 Payne D. J. B., Melatos A., 2006, ApJ, 641, 471  
 Payne D. J. B., Melatos A., 2007, MNRAS, 376, 609  
 Peralta C., Melatos A., Giacobello M., Ooi A., 2008, preprint (astro-ph/0805.2061), 805  
 Pons J. A., Geppert U., 2007, A&A, 470, 303  
 Potekhin A. Y., 1999, A&A, 351, 787  
 Potekhin A. Y., Baiko D. A., Haensel P., Yakovlev D. G., 1999, A&A, 346, 345  
 Press W. H., Flannery B. P., Teukolsky S. A., 1986, Numerical recipes. The art of scientific computing. Cambridge: University Press, 1986  
 Romani R. W., 1990, Nature, 347, 741  
 Schatz H., Bildsten L., Cumming A., Wiescher M., 1999, ApJ, 524, 1014  
 Schindler K., Hesse M., Birn J., 1988, J. Geophys. Res., 93, 5547  
 Singh S., Tandon J. N., 1969, Journal of Plasma Physics, 3, 633  
 Spitkovsky A., Levin Y., Ushomirsky G., 2002, ApJ, 566, 1018  
 Stone J. M., 1999, J. Comput. Appl. Math., 109, 261  
 Taam R. E., van de Heuvel E. P. J., 1986, ApJ, 305, 235  
 Ushomirsky G., Cutler C., Bildsten L., 2000, MNRAS, 319,

902

van den Heuvel E. P. J., Bitzaraki O., 1995, *A&A*, 297, L41+

Vigeliu M., 2008, PhD thesis, School of Physics. University of Melbourne.

Vigeliu M., Melatos A., 2008a, *MNRAS*(submitted)

Vigeliu M., Melatos A., 2008b, *MNRAS*(submitted)

Vigeliu M., Melatos A., 2008c, *MNRAS*, 386, 1294

von Neumann J., Richtmyer R. D., 1950, *J. Appl. Phys.*, 21, 232

## APPENDIX A: IMPLEMENTING RESISTIVITY IN ZEUS-MP

### A1 Advection step

Resistive MHD comprises a set of seven coupled, nonlinear partial differential equations for the magnetic field  $\mathbf{B}$ , the bulk velocity  $\mathbf{v}$ , the plasma density  $\rho$ , and the pressure  $p$  (Goedbloed & Poedts 2004): the equation of mass conservation,

$$\frac{\partial \rho}{\partial t} + \nabla \cdot (\rho \mathbf{v}) = 0, \quad (\text{A1})$$

the momentum equation,

$$\rho \left( \frac{\partial \mathbf{v}}{\partial t} + \mathbf{v} \cdot \nabla \mathbf{v} \right) + \nabla p - (\nabla \times \mathbf{B}) \times \mathbf{B} + \rho \nabla \varphi = 0, \quad (\text{A2})$$

and the induction equation,

$$\frac{\partial \mathbf{B}}{\partial t} - \nabla \times (\mathbf{v} \times \mathbf{B} - \eta \nabla \times \mathbf{B}) = 0, \quad (\text{A3})$$

where  $\eta$  denotes the resistivity and  $\varphi$  is the gravitational field. The system is closed by the supplementary condition  $\nabla \cdot \mathbf{B} = 0$  and an isothermal equation of state  $p = c_s^2 \rho$ , where  $c_s$  represents the isothermal sound speed.

As explained by Hayes et al. (2006), ZEUS-MP employs an operator split algorithm based on the method of finite differences on a staggered grid. The advection step is done in two stages. Firstly, a source step solves

$$\rho \frac{\partial \mathbf{v}}{\partial t} = -\nabla p - \nabla \cdot \mathbf{Q} - \rho \nabla \varphi - \nabla (B^2/2\mu_0), \quad (\text{A4})$$

where an artificial viscous pressure tensor  $\mathbf{Q}$  is included (von Neumann & Richtmyer 1950). Secondly, to treat transversal MHD waves properly, one must solve the magnetic tension force along with the induction equation in a single step using the method of characteristics and constrained transport (MOCCT) (Hawley & Stone 1995). The MOCCT step advances  $\mathbf{B}$  by computing the line integral of the electromotive force (EMF)  $\boldsymbol{\epsilon} = \mathbf{v} \times \mathbf{B}$  around a cell boundary  $S$ :

$$\frac{d}{dt} \int_S \mathbf{B} \cdot d\mathbf{S} = \oint_{\partial S} \boldsymbol{\epsilon} \cdot d\mathbf{l}. \quad (\text{A5})$$

Second-order accuracy in time is achieved by employing time-centered values for  $\boldsymbol{\epsilon}$ . The extrapolation in time is done using the characteristic equation for transverse Alfvén waves. It can be shown that MOCCT ensures  $\nabla \cdot \mathbf{B} = 0$  to machine accuracy at all times provided the initial field is solenoidal. The extrapolated  $\mathbf{B}$  is then used to work out the transverse magnetic forces and accelerate the fluid accordingly:

$$\rho \frac{\partial \mathbf{v}}{\partial t} \Big|_{\text{final}} = \frac{\partial \mathbf{v}}{\partial t} \Big|_{\text{sourcestep}} + \mu_0^{-1} (\mathbf{B} \cdot \nabla) \mathbf{B}. \quad (\text{A6})$$

Finally, the fluid density and momentum are advected via

$$\frac{d}{dt} \int_V \rho dV = - \oint_{\partial V} \rho \mathbf{v} \cdot d\mathbf{S} \quad (\text{A7})$$

and

$$\frac{d}{dt} \int_V \rho \mathbf{v} dV = - \oint_{\partial V} \rho \mathbf{v} \mathbf{v} \cdot d\mathbf{S}. \quad (\text{A8})$$

A visual comparison of (A3) and (A5) suggests a natural way to incorporate the resistive term (Stone 1999): we use the updated  $\mathbf{B}$  to work out the current density  $\mathbf{j} = \nabla \times \mathbf{B}$  and apply equation (A5) again, replacing  $\boldsymbol{\epsilon}$  by  $-\eta \mathbf{j}$  this time. The staggered grid allows for central differencing and thereby guarantees spatial second-order accuracy. This resistive algorithm has been used in conjunction with ZEUS-3D to study protostellar jet formation (Fendt & Čemeljić 2002).

A von Neumann analysis in terms of eigenmodes yields a stability criterion for parabolic PDEs (Press et al. 1986),  $\Delta t \leq 2\Delta^2 \eta^{-1}$ , which depends quadratically on the minimal grid cell size  $\Delta$ . We find empirically that our implementation requires  $\Delta t \leq 10^{-2} \Delta^2 \eta^{-1}$ . If  $\eta$  is high, this constraint dominates the ideal-MHD timestep and drastically increases the run time. We therefore make use of a superstep algorithm, similar to the one described by Alexiades et al. (1996). We compute the ideal-MHD timestep  $\Delta t_{\text{CFL}}$  according to the usual Courant-Friedrichs-Lewy (CFL) condition, as well as the resistive timestep  $\Delta t_{\text{resistive}}$ . After updating  $\mathbf{B}$  by the MOCCT procedure, we apply the resistive algorithm in a cycle of  $N$  steps, such that  $\Delta t_{\text{CFL}} = N \Delta t$ , with  $\Delta t \leq \Delta t_{\text{resistive}}$ . This approach was implemented successfully in a resistive module for the PLUTO code (Mignone et al. 2007).

Special care must be taken when incorporating the boundary conditions. ZEUS-MP adds two and three ghost cells at the inner and outer boundaries, respectively, where it either sets  $\boldsymbol{\epsilon}$  according to the boundary conditions for  $\mathbf{B}$  and  $\mathbf{v}$  or communicates it at a processor boundary (inside the integration volume) via the message passing interface (MPI). The processor boundaries are set by the MPI topology, i.e. the division of the computation grid among the different processors. The staggered grid requires  $\boldsymbol{\epsilon}$  at the inner boundary, so we need to add another layer of ghost cells for  $\mathbf{B}$  and  $\mathbf{v}$  there to provide  $\boldsymbol{\epsilon}$  in all ghost cells. In order to minimize the alterations to the code, we prefer to compute (or communicate to the neighbouring processor) the whole layer of ghost cells for  $\mathbf{B}$  at the beginning of every superstep. We employ the MPI communication flow described in Hayes et al. (2006) to minimize inter-processor traffic.

### A2 Test case

We test our code extensions by simulating a purely diffusive problem. We set  $\rho = 10^9 \rho_0$  (see section 2.1) and  $\mathbf{v} = 0$  to suppress any fluid motions. Equations (A1)–(A3) then reduce to a single diffusion equation

$$\frac{\partial \mathbf{B}}{\partial t} = -\nabla \times (\eta \nabla \times \mathbf{B}), \quad (\text{A9})$$

which can be solved easily in Cartesian coordinates  $(x, y, z)$ :

$$\mathbf{B}(\mathbf{r}, t) = \frac{e^{-4\eta t}}{t} \quad (\text{A10})$$

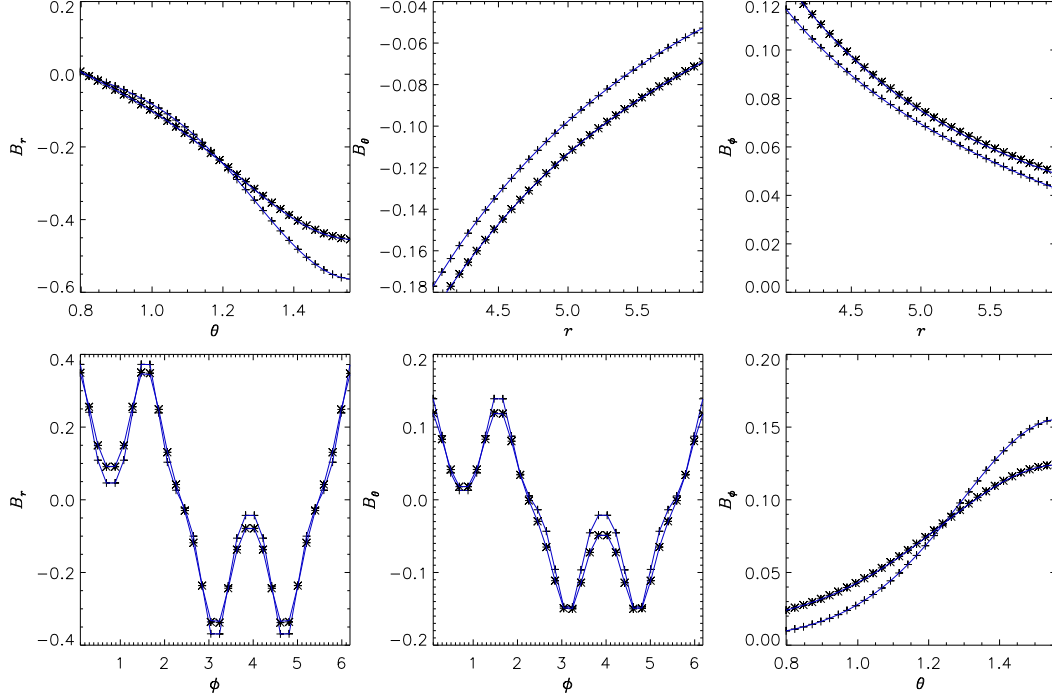


**Figure A1.** Snapshots of the three-dimensional diffusion problem in spherical coordinates at  $t = \tau_0$  (stars) and  $t = \tau_0 + 2\tau_d$  (crosses), where  $\tau_d = 0.22\tau_0$ , along with the analytic solution (A11)–(A14) (solid curves). Shown are  $B_r$ ,  $B_\theta$ , and  $B_\phi$  (left, middle, and right panels respectively) for three cross-sections:  $r = 5h_0$ ,  $\theta = 1.18$  rad, and  $\phi = 3.14$  rad. The agreement is excellent (2.4 per cent).

$$\times [e^{-(y^2+z^2)}\hat{e}_x + e^{-(x^2+z^2)}\hat{e}_y + e^{-(x^2+y^2)}\hat{e}_z].$$

A coordinate transformation yields the result in spherical coordinates:

$$B_r(\mathbf{r}, t) = \frac{e^{-\frac{r^2}{4\eta t}}}{t} \left[ e^{\frac{r^2 \cos^2 \theta}{4\eta t}} \cos \theta + \sin \theta \right. \\ \left. \times \left( e^{\frac{r^2 \cos^2 \phi \sin^2 \theta}{4\eta t}} \cos \phi + e^{\frac{r^2 \sin^2 \theta \sin^2 \phi}{4\eta t}} \sin \phi \right) \right], \quad (\text{A11})$$

$$B_\theta(\mathbf{r}, t) = \frac{e^{-\frac{r^2}{4\eta t}}}{t} [\cos \theta \quad (\text{A12})$$

$$\times \left( e^{\frac{r^2 \cos^2 \phi \sin^2 \theta}{4\eta t}} \cos \phi + e^{\frac{r^2 \sin^2 \theta \sin^2 \phi}{4\eta t}} \sin \phi \right) \\ - e^{\frac{r^2 \cos^2 \theta}{4\eta t}} \sin \theta], \quad (\text{A13})$$

and

$$B_\phi(\mathbf{r}, t) = \frac{e^{-\frac{r^2}{4\eta t}}}{t} \\ \times \left( e^{\frac{r^2 \sin^2 \theta \sin^2 \phi}{4\eta t}} \cos \phi - e^{\frac{r^2 \cos^2 \phi \sin^2 \theta}{4\eta t}} \sin \phi \right). \quad (\text{A14})$$

Test runs were performed in Cartesian (three dimensions) and spherical polar coordinates (two and three dimensions) employing time-dependent boundary conditions with Eqs. (A11) and (A14). Fig. A shows two snapshots of the three-dimensional run in spherical polar coordinates at  $t = \tau_0$  (stars) and  $t = \tau_0 + 2\tau_d$  (crosses), with  $t_d = 0.22\tau_0$ , along with the analytic solution (A11)–(A14). They are in excellent agreement, with relative error  $< 2.4$  per cent at  $t = \tau_0 + 2\tau_d$ .

## APPENDIX B: RESISTIVE PARKER INSTABILITY

In this section, we derive an analytic dispersion relation for the linear, resistive, MHD modes of a plane-parallel, gravitating plasma slab (Singh & Tandon 1969). The ideal-MHD counterpart of this problem is known as the Parker instability (Parker 1967; Mouschovias 1974).

Let us assume a uniform gravitational acceleration  $g$  directed parallel to the  $z$ -axis, and a unidirectional magnetic field parallel to the  $y$ -axis. We can then write down the magnetostatic equilibrium. The density and magnetic field are given by

$$\rho(z) = \rho_0 \exp \left[ \frac{-gz}{u^2(1+\alpha)} \right], \quad (\text{B1})$$

$$\mathbf{B}(z) = B_0 \exp \left[ \frac{-gz}{2u^2(1+\alpha)} \right] \mathbf{e}_y, \quad (\text{B2})$$

under the additional assumption that the magnetic pressure is proportional to the gas pressure everywhere, viz.

$$\frac{B^2}{2\mu_0} = \alpha p. \quad (\text{B3})$$

The equation of state is  $p = u^2 \rho$ .

Next, we write down the linearized equations of mass conservation,

$$\frac{\partial \rho^{(1)}}{\partial t} + \rho \nabla \cdot \mathbf{v}^{(1)} + \mathbf{v}^{(1)} \cdot \nabla \rho = 0, \quad (\text{B4})$$

force balance,

$$\rho \frac{\partial \mathbf{v}^{(1)}}{\partial t} = -\nabla p^{(1)} - \frac{1}{2\mu_0} \nabla [2\mathbf{B} \cdot \mathbf{B}^{(1)}] \quad (\text{B5})$$

$$+ \frac{1}{\mu_0} \mathbf{B} \cdot \nabla \mathbf{B}^{(1)} + \frac{1}{\mu_0} \mathbf{B}^{(1)} \cdot \nabla \mathbf{B} - \rho^{(1)} g \mathbf{e}_z \quad (\text{B6})$$

and induction,

$$\frac{\partial \mathbf{B}^{(1)}}{\partial t} = \frac{c^2}{4\pi\sigma} \nabla^2 \mathbf{B}^{(1)} + \nabla \times [\mathbf{v}^{(1)} \times \mathbf{B}]. \quad (\text{B7})$$

In (B4)–(B7) and below,  $p^{(1)}$ ,  $\rho^{(1)}$ ,  $\mathbf{B}^{(1)}$ , and  $\mathbf{v}^{(1)}$  denote the perturbations of the pressure, density, magnetic field, and velocity respectively.  $\sigma$  denotes the conductivity.

Ignoring interchange modes ( $k_x = 0$ ), we assume the perturbed quantities have the form  $\propto e^{i(k_y y - \omega t)}$ . Furthermore, we only consider perturbations in the  $y$ - $z$  plane, i.e.  $v_x^{(1)} = 0$  and  $\mathbf{B}^{(1)} = [0, \partial A_x^{(1)}/\partial z, -\partial A_x^{(1)}/\partial y]$ , where  $\mathbf{A} = A_x \hat{\mathbf{x}}$  is the vector potential. Eq. (B4) yields

$$-i\omega\rho^{(1)} + ik_y \rho v_y^{(1)} + \rho \frac{\partial v_z^{(1)}}{\partial z} - \frac{1}{L} v_z^{(1)} \rho = 0, \quad (\text{B8})$$

with  $L = u^2(1 + \alpha)/g$ . Similarly, the components of (B5) reduce to

$$-i\omega p v_y^{(1)} = -i u^2 k_y p^{(1)} + B_z^{(1)} \frac{\alpha u^2 \rho}{L B_y}, \quad (\text{B9})$$

and

$$-i\omega \rho v_z^{(1)} = -u^2 \frac{\partial p^{(1)}}{\partial z} - \frac{\partial A_x^{(1)}}{\partial z} \frac{\alpha u^2 \rho}{L B_y} \quad (\text{B10})$$

$$- \frac{1}{\mu_0} B_y \left[ \frac{\partial^2 A_x^{(1)}}{\partial z^2} + \frac{\partial^2 A_x^{(1)}}{\partial y^2} \right] - \rho^{(1)} g. \quad (\text{B11})$$

Finally, the induction equation (B7) yields

$$\frac{\partial A_x^{(1)}}{\partial t} = \frac{c^2}{4\pi\sigma} \left( -k_y^2 + \frac{\partial^2}{\partial z^2} \right) A_x^{(1)} - B_y v_z^{(1)}. \quad (\text{B12})$$

In order to solve (B8)–(B12) analytically, we make the short-wavelength approximation  $\partial/\partial z \ll k_y$ . Eliminating  $v_z^{(1)}$  and  $\rho^{(1)}$ , we find the dispersion relation

$$\left( \omega^2 + \frac{i\omega}{\mu_0\sigma} k_y^2 - 2\alpha u^2 k_y^2 \right) (\omega^2 - u^2 k_y^2) = \frac{g^2 \alpha}{1 + \alpha}. \quad (\text{B13})$$

For  $\sigma \rightarrow \infty$ , (B13) can be solved to obtain

$$2\omega_\infty^2 = (1 - 2\alpha) u^2 k_y^2 \pm \left[ (1 - 2\alpha)^2 u^4 k_y^4 - \frac{4k_y^2 g^2 \alpha}{1 + \alpha} \right]^{1/2}. \quad (\text{B14})$$

The modes are stable when the discriminant is positive:

$$\frac{u^4 k_y^4}{g^2} > \frac{4\alpha}{1 + \alpha} \frac{1}{(1 - 2\alpha)^2}. \quad (\text{B15})$$

For large but finite  $\sigma$ ,  $\omega_\infty$  is perturbed slightly, with  $\omega = \omega_\infty + \omega'$  and  $|\omega'| \ll \omega_\infty$ . Solving for  $\omega'$ , we obtain two branches, the first damped,

$$\omega'_{\text{damped}} = -\frac{i k_y^2 c^2}{8\pi\sigma} = -\frac{1}{2\tau_D} \quad (\text{B16})$$

and the second growing,

$$\omega'_{\text{growing}} = \frac{i c^2}{16\pi\sigma} \frac{2\alpha}{1 + \alpha} \frac{g^2}{(1 - 2\alpha)^2 u^4} \quad (\text{B17})$$

$$= \frac{1}{2(1 - 2\alpha)^2} \frac{\alpha}{1 + \alpha} \frac{g^2}{k_y^2 u^2} \frac{1}{\tau_D}. \quad (\text{B18})$$

The damped mode has a decay time roughly equal to the diffusion time  $\tau_D$ , whereas the growing mode amplifies quickly,

over the time required to diffuse across one hydrostatic scale height.